

Generation and Evolution of Fission Fragment Angular Momenta: A Global and Microscopic Study

S. Y. Chen¹, M. H. Zhou¹, Z. Y. Li^{2,1}, and Z. P. Li^{1*}

¹*School of Physical Science and Technology, Southwest University, Chongqing 400715, China*

²*China Nuclear Data Center, China Institute of Atomic Energy, Beijing 102413, China*

(Dated: November 13, 2023)

How the fission fragment angular momenta (FFAM) develop dynamically from nothing is a crucial issue in the study of fission mechanism. To this end, we construct a time-dependent generator coordinate method that includes multiple rotations of fragments and their relative motion, the coupling between rotations, as well as vibrations based on the covariant density functional theory. We investigate the generation of FFAM from the equilibrium state of the compound nucleus to a large separation of fission fragments for the first time. Remarkably, the probability distribution of FFAM exhibits a rapid fluctuation in the two-dimensional FFAM plane during the forming process of fragments and takes shape as the fragments are basically formed. The final distributions of FFAM are consistent with the experimental measurements and the sawtooth-like mass dependence of average FFAM is reproduced very well. We also find that the magnitudes of FFAM are almost uncorrelated for lower and medium angular momenta, while strong correlations of orientations at the opening angle $\phi_{\text{LH}} \approx 26^\circ$, 100° , and 160° are predicted due to the quantum fluctuations.

Introduction—The insight into the generation and evolution of fission fragment angular momenta (FFAM) is not only important for the fundamental understanding of fission mechanism, but also has consequences for a number of key problems during the deexcitation process, such as anisotropy of neutron emission [1, 2], γ -ray multiplicity and angular distribution [3–6], the γ -ray heating problem in nuclear reactors [7] and so on. From the 1960s, great efforts have been made on the experimental measurement of FFAM [8–12], and till 2021, impressive progress has been achieved by Wilson *et al.* [13]: A sawtooth-like mass dependence of FFAM with high precision was measured across three different fission reactions. The observed lack of correlation between the angular momenta of the fragment partners was interpreted as a proof of their postscission origin, which triggered a fierce discussion on the generation mechanism and dynamical evolution of FFAM [14–16].

Theoretical studies on the mechanism of FFAM are mainly based on the statistical models including statistical fluctuations and/or quantum effects [4, 16–19] and the angular momentum projection on a microscopic static/dynamic intrinsic wave function [14, 15, 20–23]. Very recently, a time-dependent collective Hamiltonian model is proposed to analyze the dynamics of FFAM during and after scission in a scheme including multiple rotations [24]. These methods can basically reproduce the distributions of FFAM and demonstrate the importance of the quantum effects and quantum fluctuations. However, one of the most important questions that is how the FFAM develop dynamically from nothing is still not understood particularly in a microscopic framework. Moreover, how the quantum fluctuations affect the correlations between FFAM needs to be further investigated. Clearly, this requires a global, dynamical,

and microscopic study that enables to describe the generation and evolution of FFAM in the whole fission process and includes as more as possible quantum fluctuations.

Here, we construct a time-dependent generator coordinate method that includes multiple rotations of fragments and their relative motion, the coupling between rotations, as well as vibrations in a large collective space based on the microscopic covariant density functional theory (CDFT), which is referred to as TD-MRV. We investigate the generation of FFAM from the equilibrium state of the compound nucleus to a large separation of fission fragments for the first time, and analyze the dynamical evolution with more quantum fluctuations. In addition, the method possesses a potential that can describe both the fission yields and distributions of FFAM in the same footing.

Theoretical Model— Low-energy nuclear fission is a slow and large-amplitude collective motion involving complicated quantum fluctuations in a series of collective degrees of freedom. The quantum fluctuations mainly represent as the shape vibrations, and can also induce collective rotations in particular when the nucleus goes beyond the saddle, where the elongation of the compound nucleus will be accelerated and the fragments are forming [25]. Figure 1 shows a schematic picture of the collective vibrations, rotations, and their combinations of a fissioning nucleus. As the nucleus further elongates, the collective rotations will gradually diverge to those of the two forming fragments and the relative rotation between them. These collective rotations are correlated with each other by the residual interactions, which can be expanded in different orders and the dominant part is the quadrupole-quadrupole interaction.

To this end, we can construct a collective Hamiltonian that contains not only the vibrations in axially symmetric quadrupole and octupole shapes β_2 , β_3 but also the rotations of two (forming) fragments and their

* E-mail: zpliphy@swu.edu.cn

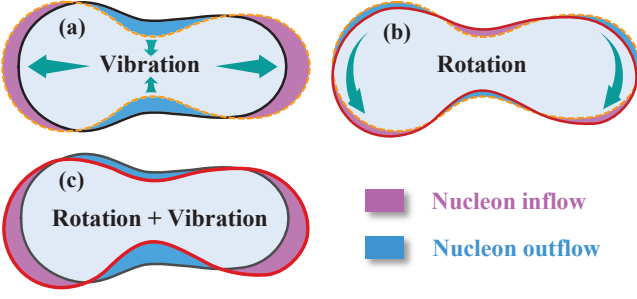


FIG. 1. Scheme of the collective vibrations (a), rotations (b), and their combinations (c) of a fissioning nucleus caused by quantum fluctuations.

relative motion:

$$\hat{H} = -\frac{\hbar^2}{2} \sum_{p,q=2,3} \frac{\partial}{\partial \beta_p} B_{pq}^{-1} \frac{\partial}{\partial \beta_q} + \sum_i \frac{\hat{S}_i^2}{2\mathcal{I}_i} + V(\beta_2, \beta_3) + \sum_{i<j} \chi_2 \hat{Q}_2^i \cdot \hat{Q}_2^j \quad (i, j = L, H, \Lambda) \quad (1)$$

where B_{pq} and V are the mass tensor and collective potential, respectively. $S_{L(H)}$ is the angular momentum of the light (heavy) fragment and S_Λ is the relative orbital angular momentum between two fragments. $\mathcal{I}_{L(H)}$ and \mathcal{I}_Λ are the corresponding moments of inertia. Before the onset of primary fragments, the rotations reduce to only the one of the mother nucleus described by \hat{S}_Λ term. χ_2 in the quadrupole-quadrupole interaction terms denotes the interaction strength. \hat{Q}_2^i is the quadrupole operator and the μ component of it takes a simple form due to the axial symmetry:

$$\hat{Q}_{2\mu}^i = D_{\mu 0}^2 q_2^i = D_{\mu 0}^2 \cdot \frac{3}{4\pi} A_i R_0^2 \beta_2^i \quad (2)$$

where $D_{\mu 0}^2$ is the Wigner D-function and q_2^i is the in-

trinsic quadrupole moment. $R_0 = r_0 A_i^{1/3}$ with $r_0 = 1.2$ fm. A_i and β_2^i denote the mass number and quadrupole deformation of the fragment ($i = L, H$) or the mother nucleus ($i = \Lambda$).

In this work, the deformation dependent mass tensor B_{pq} , moments of inertia \mathcal{I} , collective potential V , and quadrupole deformations of fragments $\beta_2^{L,H}$ are all determined microscopically by the covariant density functional theory (CDFT) with constraints on the quadrupole and octupole deformations inside the scission line and on the density distributions beyond scission under an approximation with frozen fragments [26]. The detailed expressions for the collective parameters can be found in our previous works [27, 28]. It is notable that the $\mathcal{I}_{L(H)}$ is also calculated using the Inglis-Beleyev formula [29, 30] based on the intrinsic mean-field potential of the fragment, which is deduced from its density distribution under the same CDFT framework. Details can be found in Fig. S1 in the supplemental materials.

Once the collective Hamiltonian is given, we can simulate the fission dynamics and, in particular, the generation and evolution of FFAM by performing the time evolution of a collective wave function, which takes the form

$$\sum_n \phi_n(\beta_2, \beta_3, t) |S_L S_H (S_{LH}) S_\Lambda; JM\rangle \quad n \equiv (S_L, S_H, S_\Lambda) \quad (3)$$

for a certain total angular momentum J . ϕ_n is the wave packet in the collective space of shapes and n label the different angular momentum coupling channels. Here, J is set as zero following the previous works [18, 19, 24, 31], and meanwhile, we reduce the two dimensional collective space (β_2, β_3) to a certain path with the variable β ($\delta\beta = \sqrt{\delta\beta_2^2 + \delta\beta_3^2}$) due to a fact that the collective flow in the (β_2, β_3) plane basically follows the optimal fission path and around (cf. Fig. S1 in supplemental material). Finally, we obtain a time-dependent coupled channel Schrödinger-like equation:

$$i\hbar \frac{\partial}{\partial t} \phi_n(\beta, t) = \left[-\frac{\hbar^2}{2} \frac{\partial}{\partial \beta} B^{-1}(\beta) \frac{\partial}{\partial \beta} + \sum_i \frac{S_i(S_i+1)\hbar^2}{2\mathcal{I}_i} + V(\beta) \right] \phi_n(\beta, t) + \sum_{n'} \sum_{i<j} \Gamma_{nn'}^{ij} \phi_{n'}(\beta, t) \quad (4)$$

with

$$\Gamma_{nn'}^{ij} = \chi_2 (-1)^{S'_i + S'_j + S'_k} \begin{Bmatrix} S'_i & 2 & S_i \\ S_j & S'_k & S'_j \end{Bmatrix} \langle S_i || \hat{Q}_2^i || S'_i \rangle \times \langle S_j || \hat{Q}_2^j || S'_j \rangle \delta_{S_k S'_k} \quad (k \neq i \neq j) \quad (5)$$

It is solved numerically based on the finite difference method in the collective space and the Crank-Nicolson scheme for time integration [32]. The initial state is made by boosting the static ground state along β direction to an excitation energy 1 MeV higher than the

inner fission barrier and the angular momenta satisfy $J = S_L = S_H = S_\Lambda = 0$. As the primary fragments are forming, the angular momenta S_L, S_H, S_Λ are generated gradually by the descending potential and residual quadrupole-quadrupole interactions. The angular momenta satisfy triangular rule $\Delta(S_H S_L S_\Lambda)$, and they are truncated at $30\hbar$ for S_H and S_L , and $40\hbar$ for S_Λ .

It is noted that the quadrupole-quadrupole interactions play a crucial role in the dynamics of FFAM. In principle, the interaction strength χ_2 can be extracted approximately by performing constraints on the

quadrupole deformations of the fragments based on CDFT. However, in order to show the effect of correlations on the generation and evolution of FFAM more clearly, here χ_2 is set as a Fermi form

$$\chi_2 = \frac{c}{1 + \exp[(\beta - \beta_0)/\Delta\beta]} \quad (6)$$

β_0 is beyond scission where the fragments separate by 0.5 fm [24], and $\Delta\beta = 2(\beta_0 - \beta_{sc})/4.4$. Obviously, χ_2 keeps as almost a constant c from saddle to scission and then decays rapidly. c is determined by reproducing the pattern of experimental angular momentum distribution for a chosen heavy fragment in Extended Data Fig. 4 of Ref. [13]. Here, $c = 0.048$ MeV/ b^2 is used for the induced fission of ^{240}Pu .

When fragments separate far enough, e.g. the distance between the centers of mass $d_{\text{c.m.}}^{\text{FFs}} > 23$ fm, they are fully decoupled [22], and one can calculate the probability flux for each angular momentum channel:

$$F_n = \int_{t_0}^t \mathbf{J}_n(\beta, t) dt \quad (7)$$

with the current

$$\mathbf{J}_n(\beta, t) = \frac{\hbar}{2i} \frac{1}{B(\beta)} [\phi_n^*(\beta, t) \nabla \phi_n(\beta, t) - \phi_n(\beta, t) \nabla \phi_n^*(\beta, t)] \quad (8)$$

Finally, the probability distributions FFAM in two- and one-dimension can be obtained by summing the flux with respect to other component(s)

$$P(S_i, S_j) = \sum_{S_k} F_n, \quad P(S_i) = \sum_{S_j, S_k} F_n. \quad (9)$$

Results and Discussion— Here, we take ^{240}Pu as an example to analyze the generation and evolution of FFAM. Fig. 2 (a) displays the potential energy surface (PES) in the β_2 - β_3 plane calculated by CDFT with the PC-PK1 functional [33] based on two-center harmonic oscillator basis [26]. The inner and outer fission barriers and asymmetric fission valley from $(\beta_2, \beta_3) \approx (1.3, 0.5)$ to $\approx (4.0, 2.3)$ are clearly identified, which are consistent with previous calculations using Skyrme and Gogny density functionals [34–37]. Based on the PES, the low-energy fission dynamical simulation using time-dependent generator coordinate method [38] shows that the probability flow mainly follow the optimal fission path and around (c.f. Fig. S2). Therefore, we choose three fission channels around the optimal fission path: $^{134}\text{Te}+^{106}\text{Mo}$, $^{140}\text{Xe}+^{100}\text{Zr}$, and $^{150}\text{Ce}+^{90}\text{Kr}$ as examples to perform the calculations, where six fragments spread across the region of sawtooth-like distribution of FFAM [13]. The corresponding potential energy curves (PECs) and scission configurations are shown in Fig. 2 (b). It is noted that the configurations around scission are determined in the (β_2, β_3, q_N) space [39], while the configurations beyond scission are obtained by performing density constraint calculations [26]. All the PECs

drop rapidly after the outer barrier (saddle) and then basically follow the Coulomb potential for beyond scission. The fragment information at scission are summarized in Tab. I and we find that the quadrupole deformations and moments of inertia of the heavy (light) fragments increase (decrease) gradually as the mass asymmetry increases.

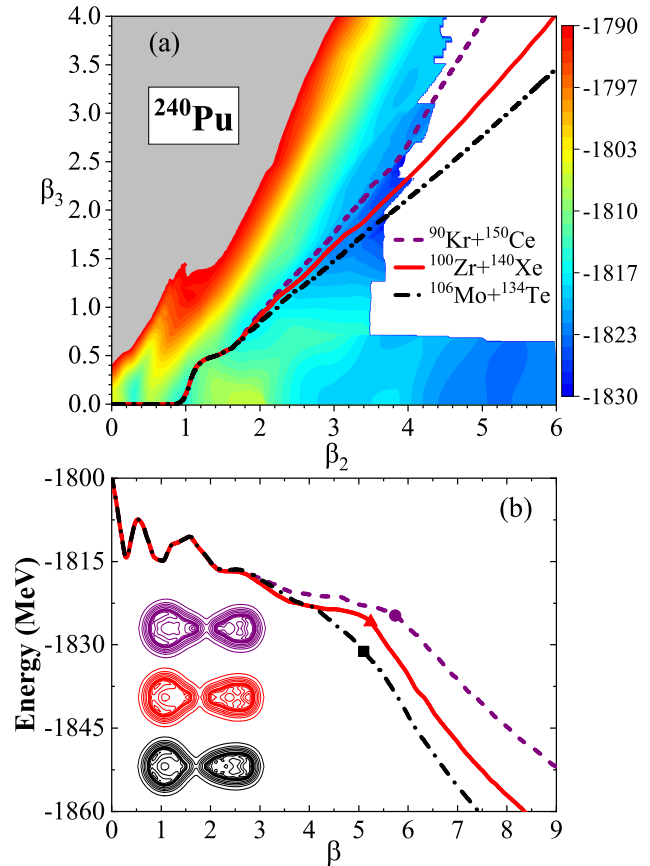


FIG. 2. (a) Potential energy surface of ^{240}Pu in the β_2 - β_3 plane calculated by CDFT with the PC-PK1 functional [33]. Three fission channels: $^{134}\text{Te}+^{106}\text{Mo}$, $^{140}\text{Xe}+^{100}\text{Zr}$, and $^{150}\text{Ce}+^{90}\text{Kr}$ are shown by the dash-dotted, solid, and dashed lines, respectively. (b) The potential energy curves and scission points (solid symbols) as functions of β for the three fission channels. The corresponding scission configurations with the nucleon number in the neck $q_N = 1$ are also shown as insets.

TABLE I. The mass numbers, quadrupole deformations, and moments of inertia of the nascent fission fragments at scission.

Fragments	Mass Number(u)	β_2^i	$\mathcal{I}_i(\hbar/\text{MeV})$
$^{134}\text{Te} (^{106}\text{Mo})$	134.18 (105.82)	0.08 (0.82)	6.30 (38.24)
$^{140}\text{Xe} (^{100}\text{Zr})$	139.90 (100.10)	0.20 (0.72)	20.20 (26.64)
$^{150}\text{Ce} (^{90}\text{Kr})$	149.53 (90.47)	0.37 (0.51)	32.08 (19.39)

With all the microscopic inputs: PEC, collective mass B (Fig. S3), moments of inertia (Fig. S4) and quadrupole deformations (Fig. S5) of the fragments, we

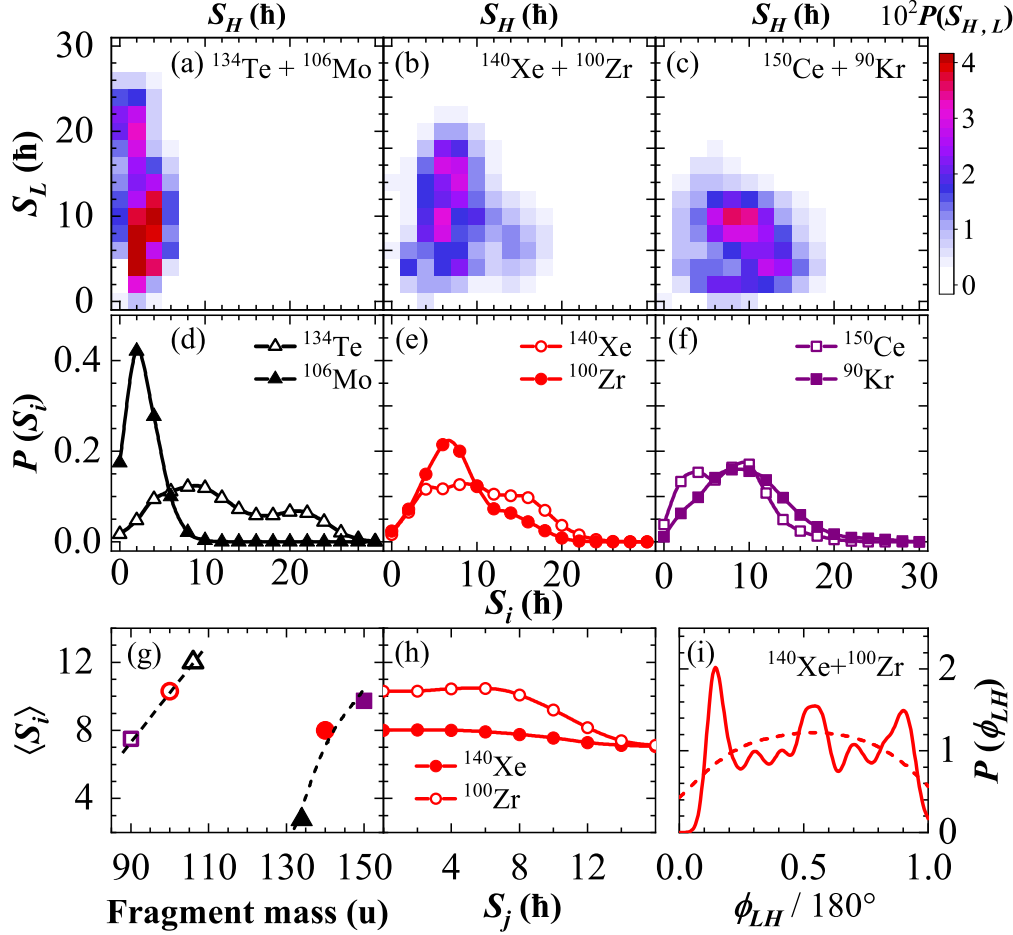


FIG. 3. (a)–(c) The probability distributions of FFAM (normalized to 100) in the S_H - S_L plane for three selected fission channels of ^{240}Pu . (d)–(f) The probability distributions of FFAM for both heavy and light fragments. (g) Mass dependence of average angular momenta for six fragments. The dashed lines are used to guide eyes. (h) Average angular momentum of ^{140}Xe (^{100}Zr) calculated using $\langle S_i \rangle = \frac{\sum_{S'_j \geq S_j} S_i P(S_i, S'_j)}{\sum_{S'_j \geq S_j} P(S_i, S'_j)}$, as function of the cutoff angular momentum S_j of the partner fragment. (i) The opening angle distribution smoothed by Gaussian convolution with $\sigma = 5^\circ$ (solid line) and $\sigma = 30^\circ$ (dashed line) for the fission channel $^{140}\text{Xe}+^{100}\text{Zr}$.

can simulate the dynamics of FFAM using Eq. 4 and the corresponding results are shown in Fig. 3. Panels (a–c), (d–f), and (g) display the two-dimensional (2D), 1D distribution of FFAM, and the mass dependence of average FFAM, respectively. Extended peaks are observed in the 2D distributions for all the three fission channels and the peaks as well as the whole pattern move toward to larger S_H as the mass asymmetry of the fragments increases. Meanwhile, the peaks shrink to lower S_L . The corresponding 1D distributions follow the trend: the peak for the heavy fragment moves from $2\hbar$ (^{134}Te) to $8-10\hbar$ (^{150}Ce) and the width extends, which are consistent with the measurements in the Extended Data Fig. 4 of Ref. [13]. Consequently, the mass dependence of average angular momenta for the six fragments presents a clear sawtooth-like pattern, which also implies positive correlations with the quadrupole deformations and moments of inertia of the nascent fragments (c.f. Tab. I).

Taking the channel $^{140}\text{Xe}+^{100}\text{Zr}$ as an example, the correlations between magnitudes and orientations of FFAM are analyzed in Figs. 3 (h), (i), respectively. The average angular momentum of ^{140}Xe (^{100}Zr) calculated using $\langle S_i \rangle = \frac{\sum_{S'_j \geq S_j} S_i P(S_i, S'_j)}{\sum_{S'_j \geq S_j} P(S_i, S'_j)}$ varies very smoothly along the cutoff S_j of the partner fragment for $S_j \leq 10\hbar$, which

is in good agreement with the experimental results [13] and indicates that the magnitudes of FFAM are almost uncorrelated. While, in Fig. 3 (i), the distribution of orientations of FFAM described by the opening angle ϕ_{LH} [16, 24] displays strong correlations at $\phi_{\text{LH}} \approx 26^\circ$, 100° , and 160° due to the quantum fluctuations. When we utilize a large smooth parameter (e.g. $\sigma = 30^\circ$) which will smooth out the quantum fluctuations, the probability distribution of opening angle becomes to a broad peak at $\phi_{\text{LH}} \approx 100^\circ$, similar to the characteristics of the classical model sampling [19, 23].

To understand how the FFAM develop from nothing to a stable distribution, we analyze the evolution of 2D FFAM distributions along the fission path from the equilibrium state of compound nucleus to a large separation of fragments for the channel $^{140}\text{Xe}+^{100}\text{Zr}$ as an example in Fig. 4. Beyond the saddle ($\beta \approx 1.60$), the elongation of the compound nucleus accelerates and the fragments are forming. Meanwhile, the potential energy drops sharply, which drives the generation and rapid fluctuation of FFAM under the residual quadrupole-quadrupole interactions, see the panels (b–i). The peak of distribution moves along the diagonal line and spreads out, and then shrinks back till $\beta = 2.36$. Subsequently, the process repeats until $\beta \approx 4.00$, where the pattern of distribution

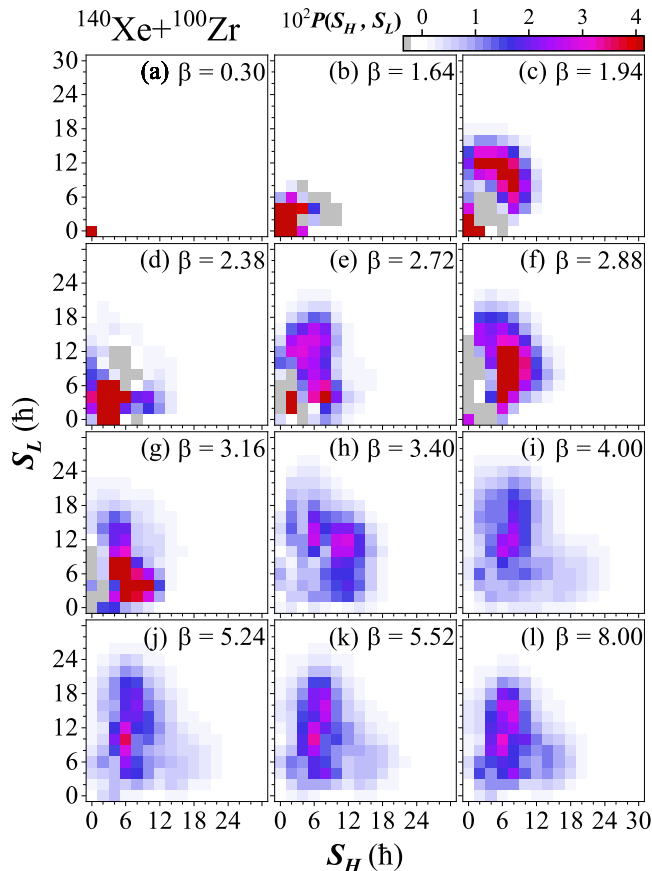


FIG. 4. The evolution of 2D FFAM distributions along the fission path from the equilibrium state of compound nucleus ($\beta \approx 0.3$) to a large separation of fragments ($\beta = 8.00$ with $d_{c.m.}^{FFs} = 23$ fm) for the channel $^{140}\text{Xe}+^{100}\text{Zr}$.

takes shape and correspondingly the major characteristics of the fragments are basically formed (c.f. Fig. S6).

From $\beta \approx 4.00$ to scission point ($\beta \approx 5.24$), the PEC varies smoothly and the peak of 2D distribution extends a little along S_L . After scission, the distribution varies slightly till to a stable pattern when the fragments are separated enough.

Summary— We have constructed the TD-MRV model that includes multiple rotations of fragments and their relative motion, the coupling between rotations, as well as vibrations in a large collective space based on the microscopic CDFT. We investigate the generation of FFAM from the equilibrium state of the compound nucleus to a large separation of fission fragments for the first time. Remarkably, the probability distribution of FFAM undergoes a rapid fluctuation in the (S_L, S_H) plane during the forming process of fragments and takes shape as the fragments are basically formed. The final distributions of FFAM are consistent with the experimental measurements and the sawtooth-like mass dependence of average FFAM is reproduced very well. The correlations between magnitudes and orientations of FFAM are also analyzed and we find that the magnitudes of FFAM are almost uncorrelated for lower and medium angular momenta, while strong correlations at the opening angle $\phi_{LH} \approx 26^\circ, 100^\circ$, and 160° are predicted due to the quantum fluctuations. Finally, we would like to emphasize that the microscopic TD-MRV model can be extended to base on two- or even multiple-dimensional potential energy surface directly that can describe not only the distributions of FFAM but also those of fission yields and total kinetic energies in the same footing.

S. Y. Chen and M. H. Zhou contributed equally to this work and should be considered as co-first authors.

Acknowledgements— This work was partly supported by the National Natural Science Foundation of China (Grants No. 12375126), the Fundamental Research Funds for the Central Universities, and the Special Fund from China Nuclear Data Center.

-
- [1] H. R. Bowman, S. G. Thompson, J. C. D. Milton, and W. J. Swiatecki, Velocity and angular distributions of prompt neutrons from spontaneous fission of cf^{252} , *Phys. Rev.* **126**, 2120 (1962).
 - [2] A. Gavron, Angular distribution of neutrons from fission fragments, *Phys. Rev. C* **13**, 2562 (1976).
 - [3] R. Albrecht, W. Dünneweber, G. Graw, H. Ho, S. G. Steadman, and J. P. Wurm, Tangential friction in deep-inelastic scattering of ^{16}O from nickel, *Phys. Rev. Lett.* **34**, 1400 (1975).
 - [4] R. Vogt and J. Randrup, Improved modeling of photon observables with the event-by-event fission model *freya*, *Phys. Rev. C* **96**, 064620 (2017).
 - [5] R. A. Dayras, R. G. Stokstad, C. B. Fulmer, D. C. Hensley, M. L. Halbert, R. L. Robinson, A. H. Snell, D. G. Sarantites, L. Westerberg, and J. H. Barker, Randomly oriented angular momentum in strongly damped collisions, *Phys. Rev. Lett.* **42**, 697 (1979).
 - [6] N. P. Giha, S. Marin, J. A. Baker, I. E. Hernandez, K. J. Kelly, M. Devlin, J. M. O'Donnell, R. Vogt, J. Randrup, P. Talou, I. Stetcu, A. E. Lovell, O. Litaize, O. Serot, A. Chebboubi, C.-Y. Wu, S. D. Clarke, and S. A. Pozzi, Correlations between energy and γ -ray emission in $\text{pu}^{239}(\text{n}, \text{f})$, *Phys. Rev. C* **107**, 014612 (2023).
 - [7] G. Rimpault, D. Bernard, D. Blanchet, C. Vaglio-Gaudard, S. Ravaux, A., and Santamarina, Needs of accurate prompt and delayed γ -spectrum and multiplicity for nuclear reactor designs, *Physics Procedia* **31**, 3 (2012).
 - [8] P. Armbruster, H. Labus, and K. Reichelt, Investigation on the primary spins of the ^{235}u fission fragments, *Zeitschrift für Naturforschung A* **26**, 512 (1971).
 - [9] F. Pleasonton, Prompt γ -rays emitted in the thermal-neutron induced fission of ^{233}u and ^{239}pu , *Nuclear Physics A* **213**, 413 (1973).
 - [10] S. A. Johansson, Gamma de-excitation of fission frag-

- ments: (i). prompt radiation, *Nuclear Physics* **60**, 378 (1964).
- [11] P. Glässel, R. Schmid-Fabian, D. Schwalm, D. Habs, and H. Helmolt, 252cf fission revisited — new insights into the fission process, *Nuclear Physics A* **502**, 315 (1989).
- [12] J. B. Wilhelmy, E. Cheifetz, R. C. Jared, S. G. Thompson, H. R. Bowman, and J. O. Rasmussen, Angular momentum of primary products formed in the spontaneous fission of ^{252}Cf , *Phys. Rev. C* **5**, 2041 (1972).
- [13] J. N. N. Wilson, D. Thisse, M. Lebois, N. Jovančević, D. Gjestvang, R. Canavan, M. Rudigier, D. Etasse, R.-B. Gerst, L. Gaudefroy, E. Adamska, P. Adsley, A. Algora, M. Babo, K. Belvedere, J. Benito, G. Benzoni, A. Blazhev, A. Boso, S. Bottoni, M. Bunce, R. Chakma, N. Cieplicka-Oryńczak, S. Courtin, M. L. Cortés, P. Davies, C. Delafosse, M. Fallot, B. Fornal, L. Fraile, A. Gottardo, V. Guadilla, G. Häfner, K. Hauschild, M. Heine, C. Henrich, I. Homm, F. Ibrahim, L. W. Iskra, P. Ivanov, S. Jazrawi, A. Korgul, P. Koseoglou, T. Kröll, T. Kurtukian-Nieto, L. Le Meur, S. Leoni, J. Ljungvall, A. Lopez-Martens, R. Lozeva, I. Matea, K. Miernik, J. Nemer, S. Oberstedt, W. Paulsen, M. Piersa, Y. Popovitch, C. Porzio, L. Qi, D. Ralet, P. H. Regan, K. Rezykina, V. Sánchez-Tembleque, S. Siem, C. Schmitt, P.-A. Söderström, C. Sürder, G. Tocabens, V. Vedia, D. Verney, N. Warr, B. Wasilewska, J. Wiederhold, M. Yavahchova, F. Zeiser, and S. Ziliani, Angular momentum generation in nuclear fission, *Nature* **590**, 566 (2021).
- [14] A. Bulgac, I. Abdurrahman, K. Godbey, and I. Stetcu, Fragment intrinsic spins and fragments' relative orbital angular momentum in nuclear fission, *Phys. Rev. Lett.* **128**, 022501 (2022).
- [15] P. Marević, N. Schunck, J. Randrup, and R. Vogt, Angular momentum of fission fragments from microscopic theory, *Phys. Rev. C* **104**, L021601 (2021).
- [16] J. Randrup and R. Vogt, Generation of fragment angular momentum in fission, *Phys. Rev. Lett.* **127**, 062502 (2021).
- [17] J. Randrup and R. Vogt, Refined treatment of angular momentum in the event-by-event fission model freya, *Phys. Rev. C* **89**, 044601 (2014).
- [18] J. Randrup, T. Døssing, and R. Vogt, Probing fission fragment angular momenta by photon measurements, *Phys. Rev. C* **106**, 014609 (2022).
- [19] J. Randrup, Coupled fission fragment angular momenta, *Phys. Rev. C* **106**, L051601 (2022).
- [20] L. Bonneau, P. Quentin, and I. N. Mikhailov, Scission configurations and their implication in fission-fragment angular momenta, *Phys. Rev. C* **75**, 064313 (2007).
- [21] G. F. Bertsch, T. Kawano, and L. M. Robledo, Angular momentum of fission fragments, *Phys. Rev. C* **99**, 034603 (2019).
- [22] A. Bulgac, I. Abdurrahman, S. Jin, K. Godbey, N. Schunck, and I. Stetcu, Fission fragment intrinsic spins and their correlations, *Phys. Rev. Lett.* **126**, 142502 (2021).
- [23] A. Bulgac, Angular correlation between the fission fragment intrinsic spins, *Phys. Rev. C* **106**, 014624 (2022).
- [24] G. Scamps and G. Bertsch, Generation, dynamics, and correlations of the fission fragments' angular momenta, *Phys. Rev. C* **108**, 034616 (2023).
- [25] C. L. Zhang, B. Schuetrumpf, and W. Nazarewicz, Neutron localization and fragment formation in nuclear fission, *Phys. Rev. C* **94**, 064323 (2016).
- [26] Z. Y. Li, S. Y. Chen, M. H. Zhou, Y. J. Chen, and Z. P. Li, Covariant density functional theory for nuclear fission based on two-center harmonic oscillator basis, arXiv , 2309.03461 (2023).
- [27] Z. P. Li, T. Nikšić, D. Vretenar, J. Meng, G. A. Lalazissis, and P. Ring, Microscopic analysis of nuclear quantum phase transitions in the $N \approx 90$ region, *Phys. Rev. C* **79**, 054301 (2009).
- [28] H. Tao, J. Zhao, Z. P. Li, T. Nikšić, and D. Vretenar, Microscopic study of induced fission dynamics of ^{226}Th with covariant energy density functionals, *Phys. Rev. C* **96**, 024319 (2017).
- [29] D. R. Inglis, Nuclear moments of inertia due to nucleon motion in a rotating well, *Phys. Rev.* **103**, 1786 (1956).
- [30] S. Beliaev, Concerning the calculation of the nuclear moment of inertia, *Nuclear Physics* **24**, 322 (1961).
- [31] G. Scamps, Microscopic description of the torque acting on fission fragments, *Phys. Rev. C* **106**, 054614 (2022).
- [32] H. Goutte, J. F. Berger, P. Casoli, and D. Gogny, Microscopic approach of fission dynamics applied to fragment kinetic energy and mass distributions in, *Phys. Rev. C* **71**, 024316 (2005).
- [33] P. W. Zhao, Z. P. Li, J. M. Yao, and J. Meng, New parametrization for the nuclear covariant energy density functional with a point-coupling interaction, *Phys. Rev. C* **82**, 054319 (2010).
- [34] D. Regnier, N. Dubray, N. Schunck, and M. Verrière, Fission fragment charge and mass distributions in $^{239}\text{Pu}(n, f)$ in the adiabatic nuclear energy density functional theory, *Phys. Rev. C* **93**, 054611 (2016).
- [35] N. Schunck and L. M. Robledo, Microscopic theory of nuclear fission: A review, *Rep. Prog. Phys.* **79**, 10.1088/0034-4885/79/11/116301 (2016).
- [36] P. Marević and N. Schunck, Fission of ^{240}Pu with symmetry-restored density functional theory, *Phys. Rev. Lett.* **125**, 102504 (2020).
- [37] Y.-J. Chen, Y. Su, G. Dong, L.-L. Liu, Z. Ge, and X. Wang, Energy density functional analysis of the fission properties of ^{240}Pu : The effect of pairing correlations *, *Chin. Phys. C* **46**, 024103 (2022).
- [38] D. Regnier, N. Dubray, M. Verrière, and N. Schunck, Felix-2.0: New version of the finite element solver for the time dependent generator coordinate method with the gaussian overlap approximation, *COMPUTER PHYSICS COMMUNICATIONS* **225**, 180 (2018).
- [39] M.-H. Zhou, Z.-Y. Li, S.-Y. Chen, Y.-J. Chen, and Z.-P. Li, Three-dimensional potential energy surface for fission of ^{236}U within covariant density functional theory, *Chinese Physics C* **47**, 064106 (2023).

Supplemental Materials

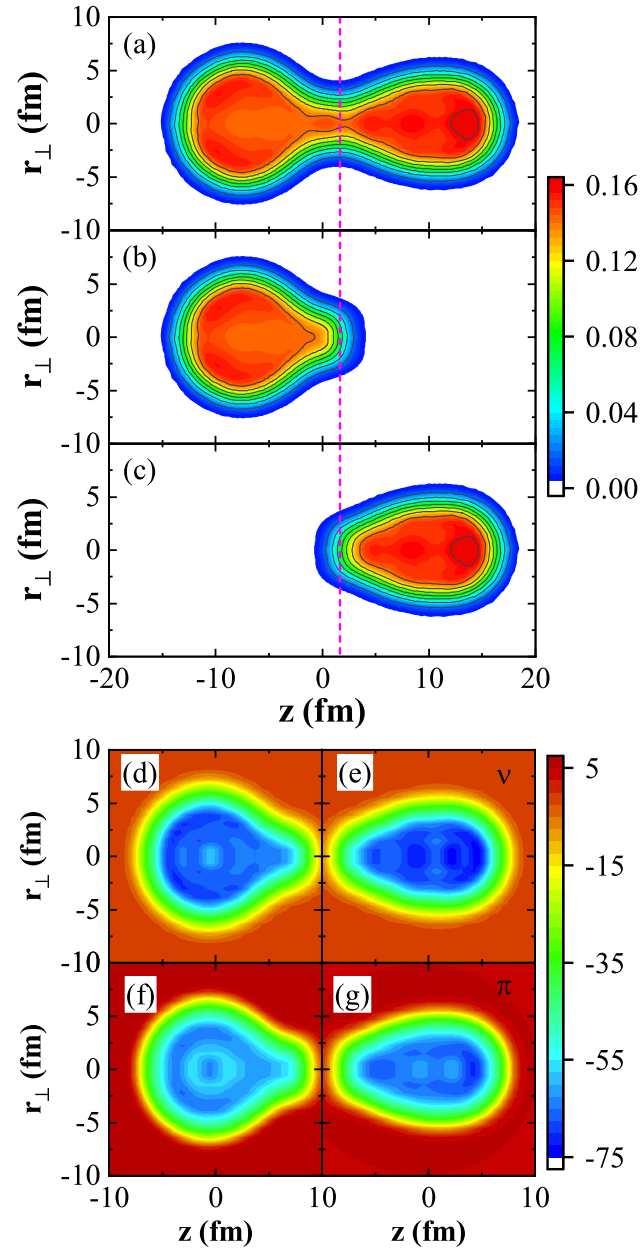


FIG. S1. (a) The nucleon density distribution of fissioning compound nucleus ^{240}Pu . (b) The density distributions for the left fission fragment extracted from that of compound nucleus using a Fermi distribution $f(z) = \frac{1}{1 + \exp[(z - z_0)/a]}$ with the neck position z_0 and diffuseness $a = 0.67$ fm. (c) Same as panel (b) but for the right fragment with a Fermi distribution $1 - f(z)$. (d-g) The neutron and proton intrinsic mean-field potentials for fission fragments determined by the corresponding densities using the same energy density functional as the whole nucleus.

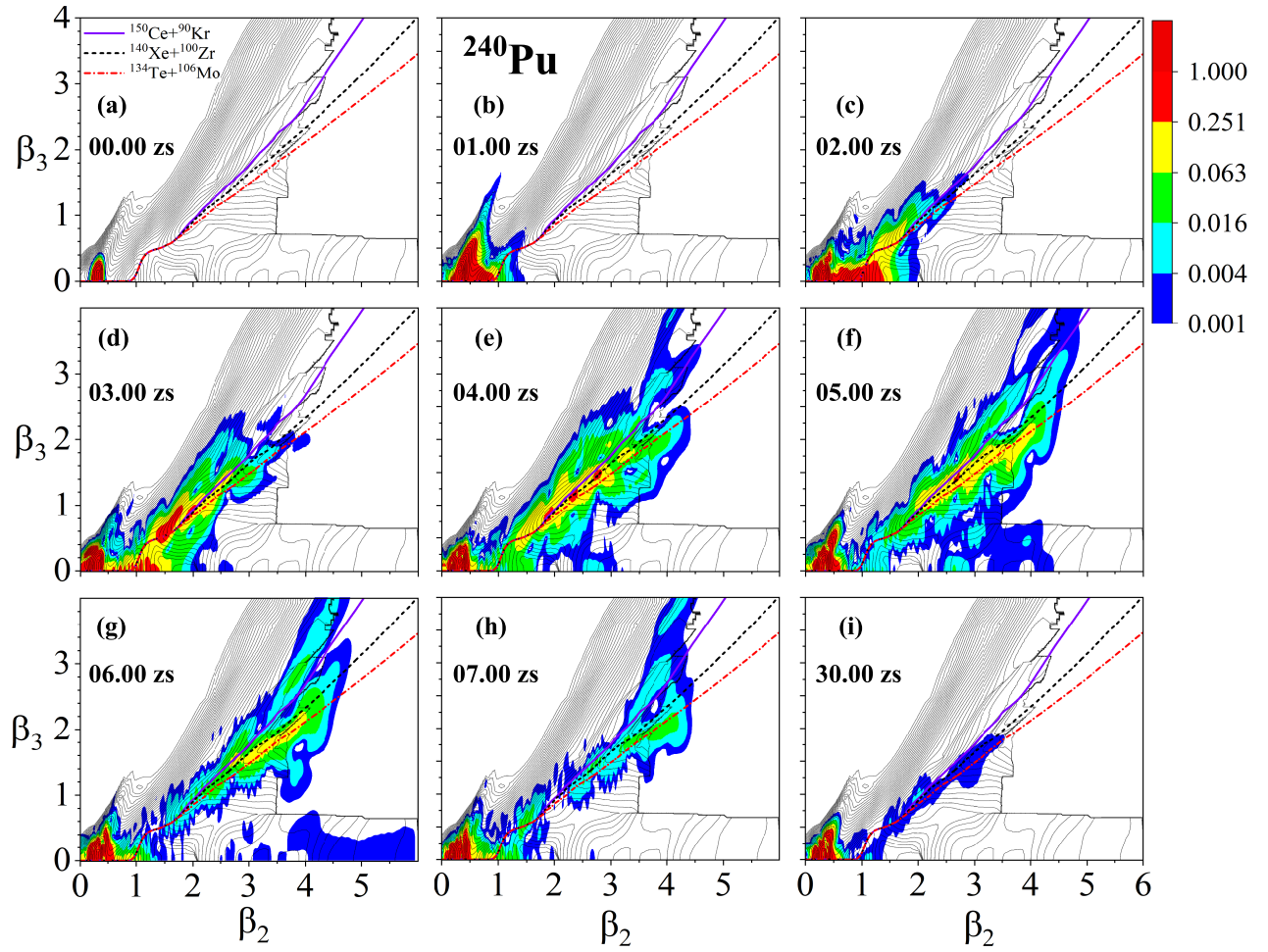


FIG. S2. Evolution of collective probability density distribution in the $\beta_2 - \beta_3$ plane for ^{240}Pu simulated by the time-dependent generator coordinate method [38].

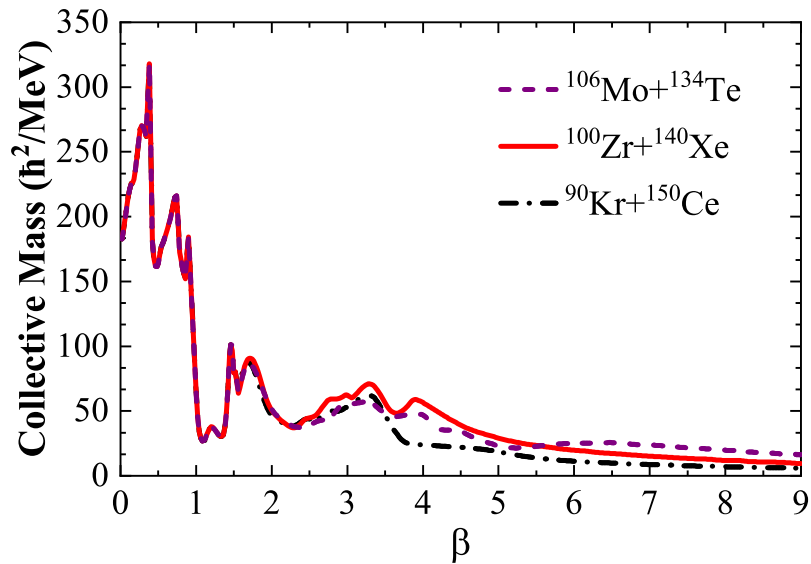


FIG. S3. The collective masses for the three fission channels as functions of β .

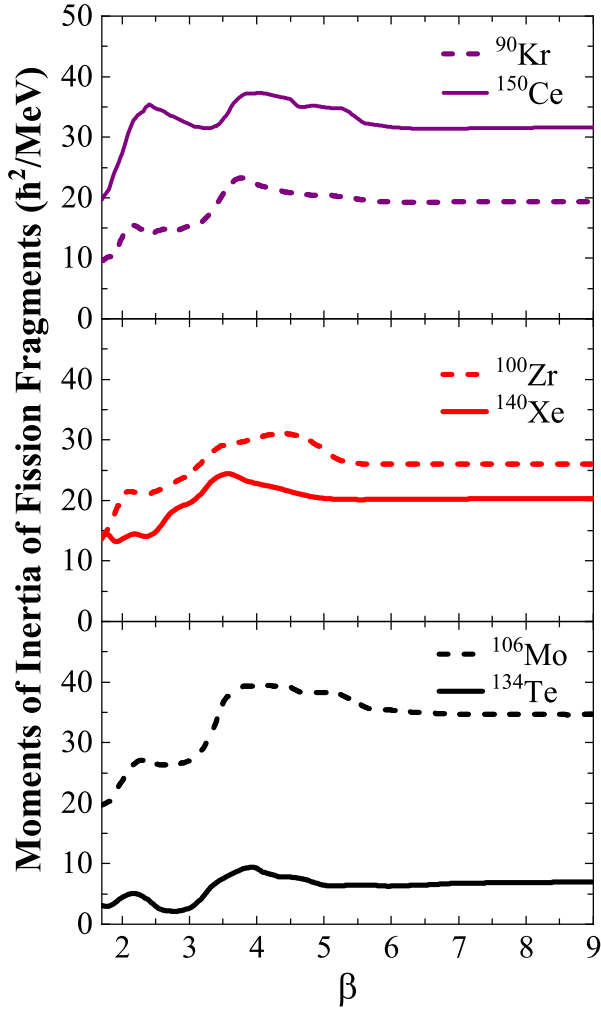


FIG. S4. Moments of inertia of fission fragments as functions of β .

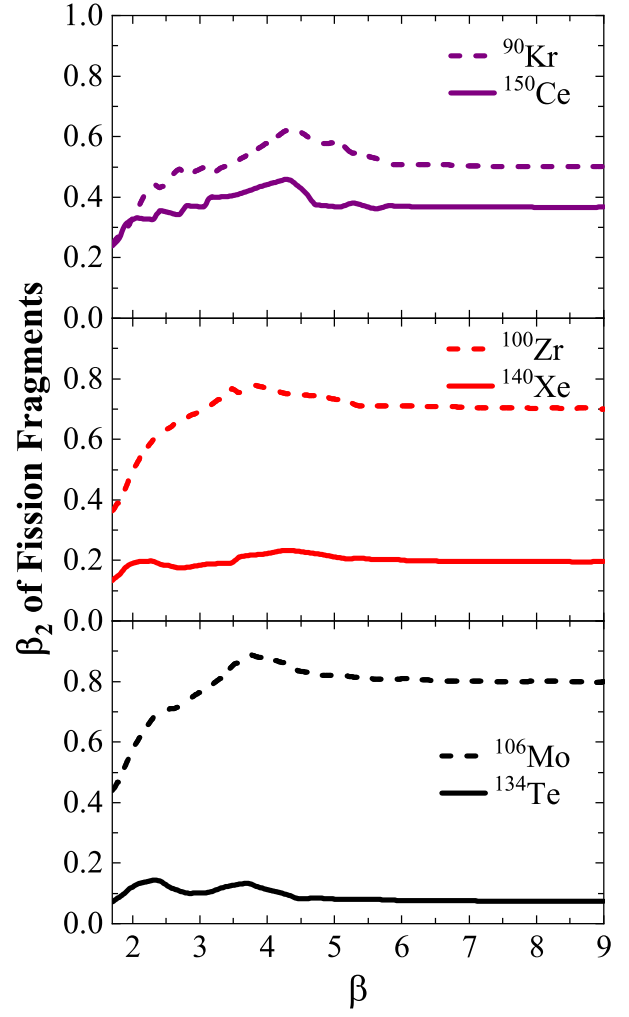


FIG. S5. Quadrupole deformations β_2 of fission fragments as functions of β .

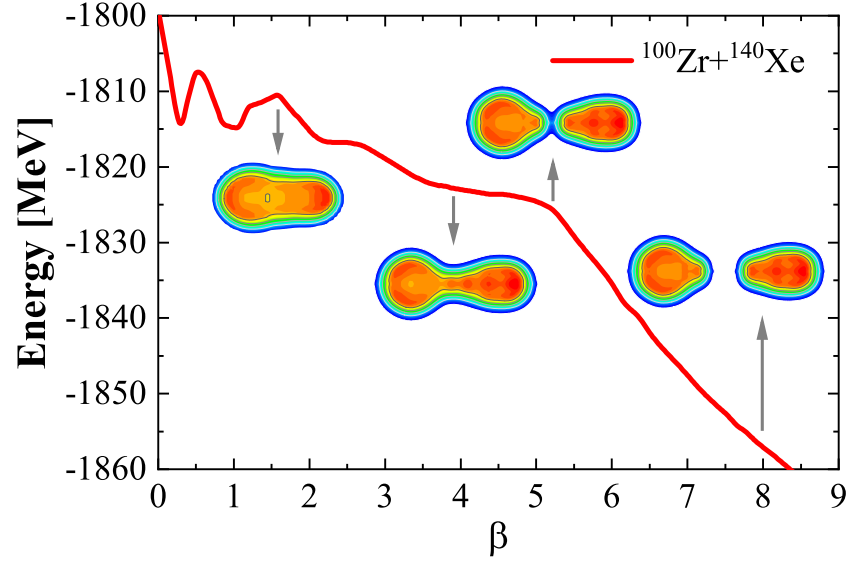


FIG. S6. PEC for the fission channel $^{240}\text{Pu} \rightarrow ^{140}\text{Xe} + ^{100}\text{Zr}$. The nucleon density distributions for the saddle ($\beta \approx 1.6$), configuration with $\beta \approx 4.0$, scission ($\beta \approx 5.24$), and configuration with large separation between two fragments are also shown.